AGU PUBLICATIONS

JGR

Journal of Geophysical Research: Space Physics

RESEARCH ARTICLE
10.1002/2015JA021830

Key Points:
- Solar wind data voids treatment
- Enhanced fluctuation power spectral analysis
- Over five decades of frequency recovery spectral range

Supporting Information:
- Supporting Information S1

Correspondence to:
D. Tordella,
daniela.tordella@polito.it

Citation:
Gallana, L., F. Fraternale, M. Iovieno, S. M. Fosson, E. Magli, M. Opher, J. D. Richardson, and D. Tordella (2016), Voyager 2 solar plasma and magnetic field spectral analysis for intermediate data sparsity, *J. Geophys. Res. Space Physics*, *121*, 3905–3919, doi:10.1002/2015JA021830.

Received 19 AUG 2015
Accepted 7 MAY 2016
Accepted article online 14 MAY 2016
Published online 31 MAY 2016

Voyager 2 solar plasma and magnetic field spectral analysis for intermediate data sparsity

Luca Gallana[1], Federico Fraternale[1], Michele Iovieno[1], Sophie M. Fosson[2], Enrico Magli[2], Merav Opher[3], John D. Richardson[4], and Daniela Tordella[1]

[1]Dipartimento di Ingegneria Meccanica e Aerospaziale, Politecnico di Torino, Torino, Italy, [2]Dipartimento di Elettronica e Telecomunicazioni, Politecnico di Torino, Torino, Italy, [3]Astronomy Department, Boston University, Boston, Massachusetts, USA, [4]Kavli Institute for Astrophysics and Space Research, Massachusetts Institute of Technology, Cambridge, Massachusetts, USA

Abstract The Voyager probes are the furthest, still active, spacecraft ever launched from Earth. During their 38 year trip, they have collected data regarding solar wind properties (such as the plasma velocity and magnetic field intensity). Unfortunately, a complete time evolution of the measured physical quantities is not available. The time series contains many gaps which increase in frequency and duration at larger distances. The aim of this work is to perform a spectral and statistical analysis of the solar wind plasma velocity and magnetic field using Voyager 2 data measured in 1979, when the gap density is between the 30% and 50%. For these gap densities, we show the spectra of gapped signals inherit the characteristics of the data gaps. In particular, the algebraic decay of the intermediate frequency range is underestimated and discrete peaks result not from the underlaying data but from the gap sequence. This analysis is achieved using five different data treatment techniques coming from the multidisciplinary context: averages on linearly interpolated subsets, correlation without data interpolation, correlation of linearly interpolated data, maximum likelihood data reconstruction, and compressed sensing spectral estimation. With five frequency decades, the spectra we obtained have the largest frequency range ever computed at five astronomical units from the Sun; spectral exponents have been determined for all the components of the velocity and magnetic field fluctuations. Void analysis is also useful in recovering other spectral properties such as micro and integral scales.

1. Introduction

The solar wind fills the heliosphere from the Sun to the termination shock with a supersonic flow of magnetized plasma. This flow is time dependent on all scales and expands with distance. The flow has fluctuations on a broad range of scales and frequencies. These fluctuations are not just convected outward but show energy cascades between the different scales. The solar wind turbulence phenomenology has been comprehensively reviewed by *Tu and Marsch* [1995]; *Bruno and Carbone* [2013].

Most studies of solar wind turbulence use data from near-Earth, with spacecraft in the ecliptic near 1 AU, see *Tu and Marsch* [1995]. Recent studies of the solar wind near 1 AU found the fluctuations in magnetic field are fit by power laws with exponents of −5/3, while those of velocity often show exponents of −3/2 [*Podesta et al.*, 2007]. The Ulysses spacecraft provided the first observations of turbulence near the solar polar regions [*Horbury and Tsurutani*, 2001]; hourly average Ulysses data show that the velocity power law exponent evolves toward −5/3 with distance from the Sun, and that spectra at 1 AU are far from the asymptotic state [*Roberts*, 2010]. In order to understand the evolution of the solar wind and its properties, it is necessary to analyze data at larger radial distances. However, data gaps typically increase with distance and make the spectral analysis challenging.

In this paper Voyager 2 (V2) plasma and magnetic field data from near 5 AU are used to study the structure of turbulence in the solar wind. Voyager 2 was launched on 23 August 1977 and reached a distance of 5 AU in the first half of 1979 (just before the Jupiter flyby. V2 closest approach to Jupiter was on July 9. We use data from 1 January to 29 June 1979 (DOY 1–180). The Voyager plasma experiment observes plasma currents in the energy/charge range 10–5950 eV/q using four modulated-grid Faraday cup detectors [*Bridge et al.*, 1977]. The observed currents are fit to convected isotropic proton Maxwellian distributions to

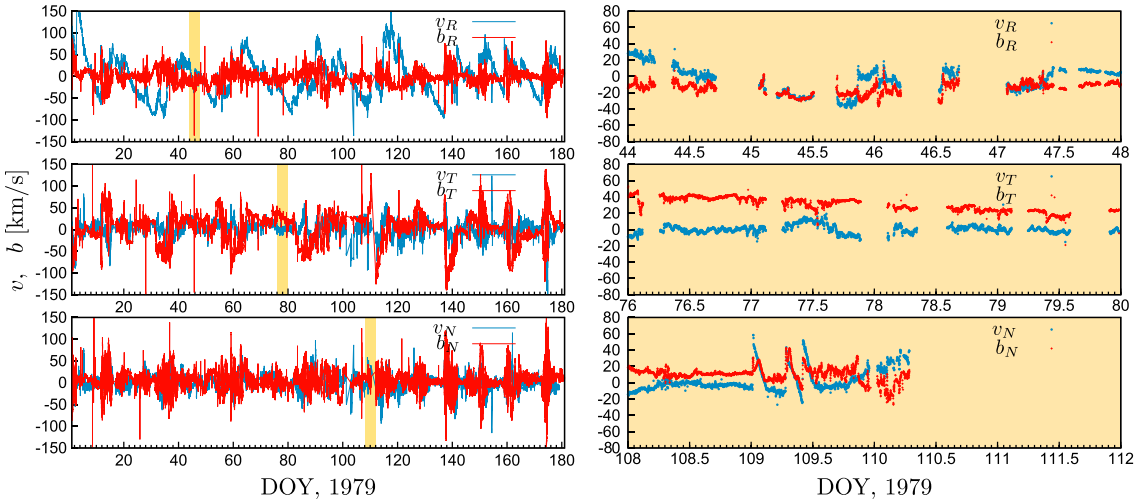

Figure 1. Voyager 2 1979 data. Plasma velocities (red lines) and magnetic fields (blue lines) recorded by Voyager 2 in the first 180 days of 1979, COHOWeb repository (http://omniweb.gsfc.nasa.gov/coho/). RTN heliographic reference frame is used. The magnetic field is represented using Alfvén units. (right column) A 4 day period is magnified to show the data gaps.

derive the parameters (velocity, density, and temperature) used in this work. Magnetic field and plasma data are from the COHOWeb repository (http://omniweb.gsfc.nasa.gov/coho/) of the NASA Goddard Space Fligh Center-Space Physics Data Facility. In 1979 data gaps are due mainly to tracking gaps; some smaller gaps are due to interference from other instruments. As a consequence, datasets from Voyager 2 are lacunous and irregularly distributed. The spectra of gapped signals of course inherit the characteristics of the data gaps. In particular, the algebraic decay of the intermediate range is underestimated and the discrete peaks are exactly located at the frequencies of the peaks in the data gap spectrum. This inheritance is negligible when the gap density is below the 10%, becomes mildly evident around a gap density of 30% and is destructive for spectrum computation when the density gap rises to 90%, which is typical inside and beyond the heliosheath. In these cases, in order to perform spectral analysis, methods for signal reconstruction of missing data must be implemented. In section 2 we present the physical behavior of the solar wind near 5 AU through statistical analysis and plasma parameters. Section three gives an overview of the signal context we work with and of the reconstruction techniques used. In section four we show and discuss the spectra analysis performed about kinetic energy, density and thermal speed. Conclusions and future development follow in section five. Supplementary Information provides practical details on the software used carry out the gapped data analysis.

2. The 1979 DOY 1 – 180 Voyager 2 Data (Probability Density Function and Intermittency; Limitation Toward Spectral Analysis)

The data set consists of vector plasma velocity and magnetic field data from 1 January 1979 00:00 GMT to 29 June 1979 19:00 GMT, a period of about 180 days, see Figure 1 and Tables 1 and 2. In 1979 the plasma speed and direction were sampled each 96 s, while for magnetic field the resolution of the data we use is 48 s (the actual sampling frequency is higher than 0.1 Hz).

As regards the magnetic field, the 48 s samples are averages from higher resolution measurements. The actual sampling time of the Voyager magnetometer is 0.06 s. From this data, 1.92 s, 9.6 s, and 48 s averages had been computed and published. As regards the plasma quantities (ion velocity, ion density, and ion thermal speed), 96 s is the sampling time in the period we consider. These data can be considered snapshots with a 96 s cadence. In detail, the plasma science instrument consists of four Faraday cups. A single measurement comes from an integration time, for each of the four detectors, which can be varied between 0.03 and 0.93 s. The time between measurements varies between 12 s and 192 s; in 1979 it was 96 s [*Behannon et al.*, 1977; *Bridge et al.*, 1977].

Table 1. Solar Wind Global Parameters[a]

	Parameter	Value
v_{SW}	Plasma velocity	$4.54 \cdot 10^2$ km/s
V_A	Alfvén velocity	$4.94 \cdot 10^1$ km/s
E_k	Kinetic energy	$2.45 \cdot 10^3$ km^2/s^2
E_m	Magnetic energy	$2.84 \cdot 10^3$ km^2/s^2
E	Total energy	$5.29 \cdot 10^7$ km^2/s^2
H_c	Cross helicity	15.8 km^2/s^2
H_m	Magnetic helicity	$2.10 \cdot 10^6$ nT^2 km
n_i	Ions numerical density	0.23 cm^{-3}
E_T	Ions thermal energy	2.29 eV
T	Ions temperature	$2.70 \cdot 10^4$ K
β_p	Plasma beta	0.22
c_s	Ions sound speed	$1.93 \cdot 10^1$ km/s
f_{ci}	Ions Larmor frequency	0.02 Hz
f_{pi}	Ions plasma frequency	0.10 kHz
r_{ci}	Ions Larmor radius	$4.29 \cdot 10^3$ km
r_i	Ion inertial radius	$1.58 \cdot 10^2$ km

[a]Reference parameters from the Voyager 2 recorded data. All the quantities are averages (or integral) over the whole period of 180 days.

It is well known that the variations in the solar wind speed reduce going outward from the Sun as fast and slow parcels push against one another. Beyond 1 AU these interaction regions form shocks and much of the solar wind at 5 AU has been shocked at least once. There is a lot of features in these time series besides turbulence (fast wind, slow wind, ejecta, shocks, sector reversals, and the heliospheric current sheet and its structures) and some of these features contribute Fourier power at all frequencies to the power spectral density.

A plot of the data is shown in Figure 1, where the fluctuations of the components of plasma velocity and magnetic field in Alfvén units are represented using the RTN Heliographic reference system. The RTN system is centered at the spacecraft, the R (radial) axis is directed radially away from the Sun through the spacecraft. The T (tangential) axis is the cross product of the Sun's spin vector (north directed) and the R axis, i.e., the T axis is parallel to the solar equatorial plane and is positive in the direction of planetary rotation around the Sun. The N (normal) axis completes the right-handed set). The right panels of the Figure 1 magnifies 4 days of data to show the typical data gap distribution.

The anisotropy of the fields can be determined by looking at the single components probability density functions (PDFs) in Figures 2a–2c. Particularly important are the differences of the radial components compared to the tangential and normal ones: a quantification of the anisotropy can be appreciated by comparing the skewness values in Table 2. The presence of intermittency in the velocity and magnetic fields can be also observed by looking at the PDFs of the modules of the normalized vector fields, shown in Figure 2d. The normalized vector fields are given by

Table 2. Intermittency and Anisotropy for the Solar Wind[a]

	μ	σ^2	Sk	Ku
v_R	454	1893	0.43	3.41
v_T	3.21	252.9	−0.99	7.35
v_N	0.51	250.3	−0.36	5.80
B_R	−30.04	0.173	0.53	6.71
B_T	0.06	0.85	−0.72	10.2
B_N	0.10	0.34	−0.24	7.65
$\lvert\delta\mathbf{v}\rvert^2$	3.00	10.47	2.40	10.27
$\lvert\delta\mathbf{B}\rvert^2$	2.48	17.41	3.17	14.90

[a]Mean values and first three moments for the velocity and magnetic fields flucutation components and their modules; μ is the mean value, σ^2 the variance, Sk the skewness and Ku the kurtosis. Velocity is measured in km/s and the magnetic field in nanotesla. The modules of the fluctuations are normalized on the variance, see equation (1), in order to be able to compare them with a chi-square distribution (standard three-component chi-square distribution has mean 3, variance 6, skewness 1.63, and kurtosis 7).

$$|\delta\mathbf{x}|^2 = \sum_i^3 \frac{(x_i - \mu_i)^2}{\sigma_i^2} \qquad (1)$$

where μ_i is the mean value and σ_i^2 the variance of the ith component of the vector field $\mathbf{x}$. The same plot shows a three-component chi-square distribution as a reference. Intermittency occurs over a broad range of scales and seems to be slightly higher in the magnetic field data which has larger skewness and kurtosis (see Table 2).

In order to analyze anisotropic effects from a spectral point of view, it is

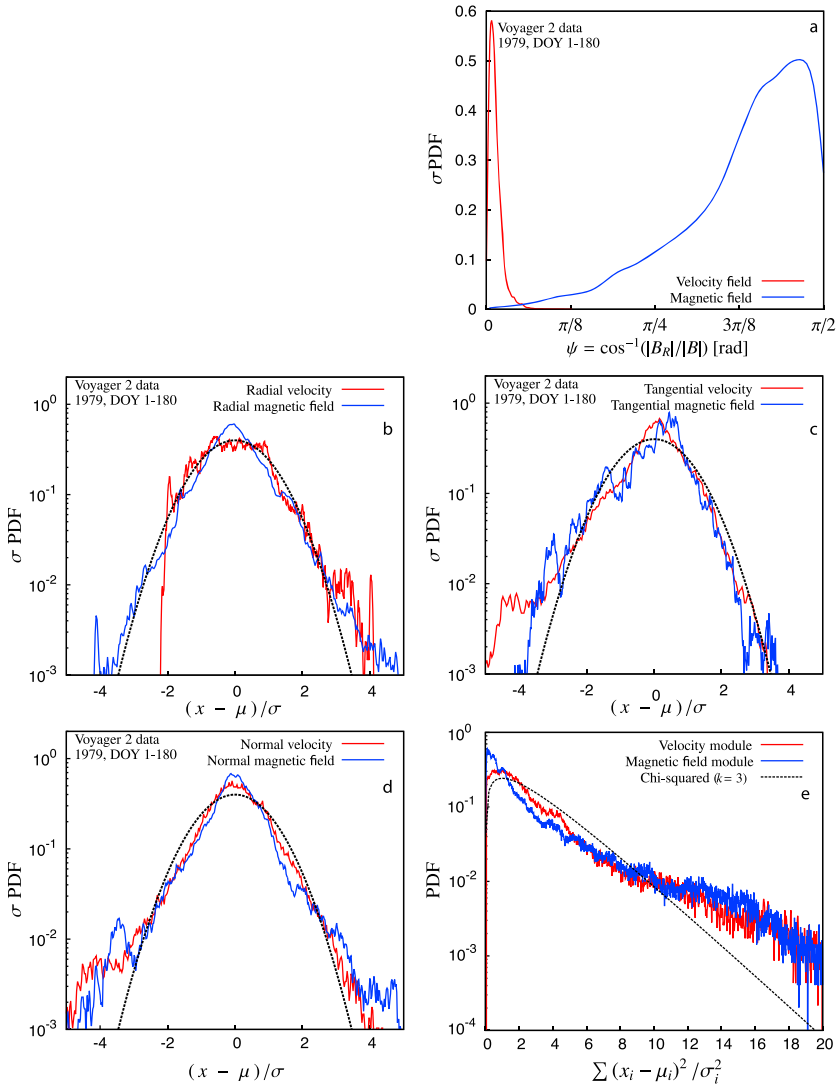

Figure 2. Probability density functions of the plasma velocity and magnetic field fluctuations. (a) Normalized probability density function of the angle ψ between the radial direction and the local velocity (red line) and magnetic (blue line) fields. The magnetic field is generally tilted 85 to 105° with respect to the radial direction. (b–d) Normalized probability density function of the plasma velocity and magnetic field components in the radial (Figure 2b), tangential (Figure 2c), and normal (Figure 2d) directions, and of their module (Figure 2e), normalized as in equation (1).

important to identify the wavenumbers parallel to the magnetic field $k_{\|}$ and normal to it $k_{\perp}$, as suggested first by *Montgomery et al.* [1987]. We consider the angle ψ between the local vector field and the radial direction, defined as

$$\psi_v = \cos^{-1}\left(\frac{|v_r|}{|\mathbf{v}|}\right) \qquad \psi_m = \cos^{-1}\left(\frac{|B_r|}{|\mathbf{B}|}\right). \tag{2}$$

The PDFs of these angles are represented in Figure 2a: while the average plasma velocity is oriented along the radial direction (the mean angle is 0.04 ± 0.03 radiant), moving away from the Sun, the magnetic field is characterized by angles close to $\pi/2$ which make it perpendicular to the radial direction as expected for a Parker spiral.

2.1. Data Gap Signal Analysis (Intermediate Level of Data Sparsity, From 30 to 50%)

The signal representing the sequence of pauses (gaps or voids) and occurrences of the flux of data information is a nondimensional temporal sequence of conventional numerical values associated with the pause status (for example, 0) and the occurrence status (for example, 1). We call this temporal sequence the *gap signal*. The sequence is a combination of random components constituted by singular events with gaps of

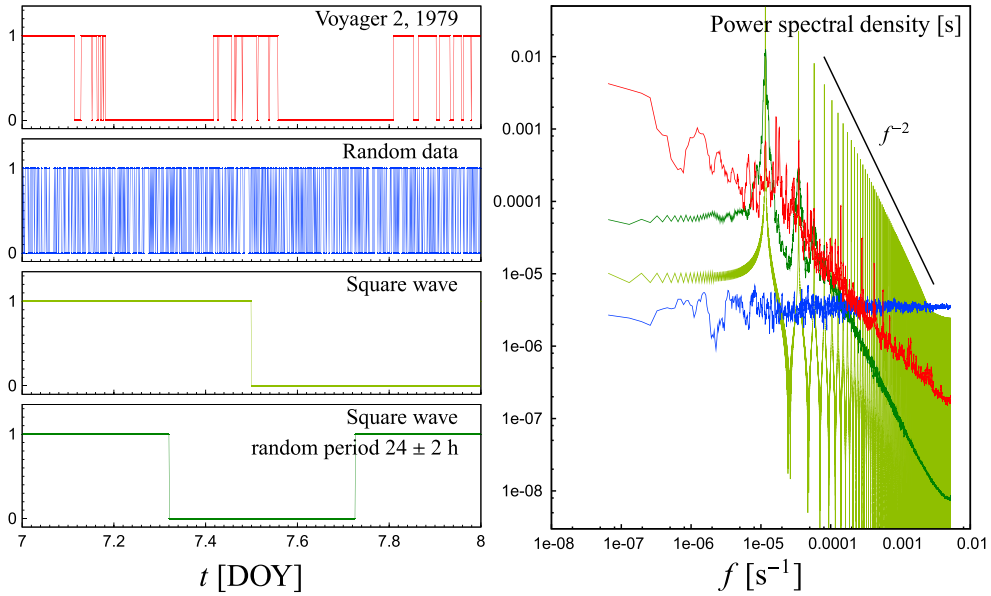

Figure 3. Spectrum of the Voyager 2 1979, DOY 1–180, gap sequence. Data gap signal (equal to 1 when the data are present and equal to 0 when the data are missing) compared with some models of gaps: random gaps, square wave, and an irregular square wave with random period (each half period has been randomly generated from a Gaussian distribution with an average of 12 h and a standard deviation of 1 h). (left column) A sample of the four signals over 1 day.

not predictable duration spaced in an irregular way and a component of periodic or near periodic events associated with the data tracking and/or acquisition and/or recovery. For example, V2 has 12 h gaps which occur because the only tracking station which can receive V2 data is the Camberra Antenna of the NASA Deep Space Network, which only can view V2 12 h/d. When we compute spectra using raw time series, the structure of the *data gap signal* enters into the power spectrum of the physical quantity under consideration. In this case, in fact, the spectrum is the convolution of the spectrum of the gap signal and of that of complete signal. A proper deconvolution numerical technique could be the solution, but we have not yet explored this possible line of investigation. Notice that this eventuality arrives when computing the correlogram by the Blackman-Tukey method (BT in the following) that estimates the power spectrum using a windowed fast Fourier transform of the autocorrelation function of the raw data time series that include gaps. In any case, it is important to know which kind of spectrum corresponds to the typical data gap signal. Computation of the relevant power spectrum shows a distribution composed of a continuous pedestal function and discrete peaks. The pedestal function features a maximum located at low frequency and an algebraic decay in the intermediate range of frequency. On top of the pedestal, one can see a distribution of a large number of discrete peaks; see 3. The data gap power spectrum has an algebraic decay exponent of about −1, which is a value midway between the zero decay shown by a random signal over the entire spectral range and the −2 decay exponent shown by the envelope of the discrete peaks associated with the harmonics of the square wave-like signal component. In fact, any data gap occurrence has a natural analogue to a switching function in time, one that is zero except during the sampling time and is unity during that time. The discrete peaks observed on top of the pedestal are due to the harmonics of the square wave-like component (a sort of switching function in time); see again Figure 3. Spectra of gapped physical signals inherit the characteristics of the data gaps; in particular, we see that the algebraic decay of the intermediate range is underestimated and the discrete peaks are located at the frequencies of the data gap spectrum. This inheritance is negligible when the gap density is below the 10%, becomes mildly evident around the 30% of gap density, and ends up to be destructive for the spectrum computation when the density gap rises to 90%, which is typical inside and beyond the Heliosheath. To achieve a general progress in the spectral postprocessing, for instance, to minimize leakage, a prewhitening treatment was associated to the BT method as applied to spectral computation of raw data time series with a low percentage of gaps (typically below 10%). Prewhitening is a method of signal decorrelation efficacious in reducing the effects induced by the presence of systematic information not

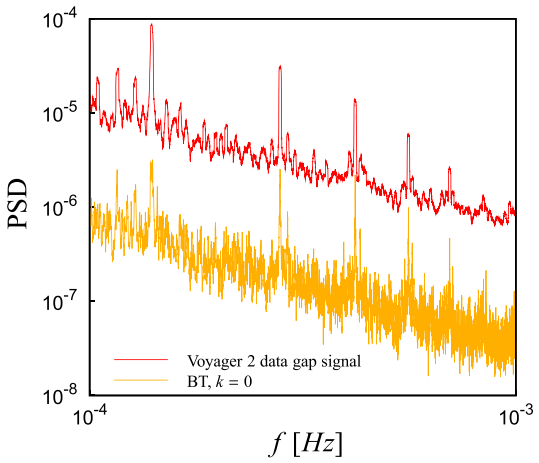

Figure 4. Inheritance of narrow spectral peaks from the data gap signal when the correlation method without any void treatment is used to compute spectra. Comparison between the power spectral density (PSD) obtained by the correlation method (Blackman-Tukey without prewhitening) on synthetic data (Synt 1) with the same gaps of Voyager 2 data and the spectrum of the data gap signal. For sake of clarity only one decade of the frequency range (10^{-4} and 10^{-3} Hz) has been shown. Arbitrary values of PSD. The coincidence of the peaks in the two cases is evident.

relevant to prediction, in a sense, something similar to the presence of periodical signal gaps. However, by its very nature the prewhitening is not efficacious in reducing the effects of the randomly distributed gaps. The use of a prewhitening filter with the parameter k in the range [0.6, 0.9] improves the results of the BT method, especially in the high-frequency range. Still spectra feature spurious peaks (see Figure 4) and biased values of the spectral index (see in supporting information Figure S1 and Table 1).

3. Methods for Spectral Analysis of Gapped Data

High data sparsity represents one of the major challenges to spectral analysis. A targeted breakthrough is to provide a simple and efficient way to obtain spectral information on the full frequency range contained in long, gappy temporal data sets in the many different plasma regimes sampled by the Voyager mission, see, e.g., two preliminary works by our group *Fraternale et al.* [2016] and *Iovieno et al.* [2016]. This advancement may in the intermediate term prepare the ground for the analysis of V2 local interstellar medium plasma data and in the long term to prepare a spectral analysis standard for observational data coming from future scientific space missions inside the interstellar medium.

Figure 5 presents the general context of gapped data treatment including details of the role played by measurement accuracy, numerical precision, presence of noise, and related energy addition. The gap distribution of the V2 velocity and magnetic field data is shown in the inset in Figure 5a. In the 180 day period analyzed, 28% and 24% of plasma and magnetic field data are missing, respectively. Naming δt the time difference between consecutive data points, the biggest gap is $\delta t_{\max} = 44.7$ h, and the total number of points is 115,102 for the velocity and density and 248,159 for the magnetic field. The longest continuous data subset lasts $T_s = 19.5$ h, and it is located at DOY 176 and 168 for plasma and magnetic fields, respectively. In the following, the temporal length of a data gap is named T_g.

In this work we have considered five methods of spectral reconstruction. These methods come from multidisciplinary areas, spanning from astrophysics (maximum likelihood), to classical numerical analysis, to telecommunication engineering and image processing (compressed sensing). The first method is limited to short intervals and, therefore, does not allow a spectral reconstruction over many decades, while the others could be applied to any time period. The methods are listed below:

1. Windowed averaged Fourier transforms of short data subsets, linearly interpolated over short gaps.
2. Fourier transform of the correlation function, the Blackman-Tukey method.
3. Fourier transform of the correlation function obtained after a linear interpolation of the data.
4. Maximum likelihood recovery by *Rybicki and Press* [1992].
5. Spectral estimation via compressed sensing [see, e.g., *Donoho*, 2006; *Candes et al.*, 2006a].

In order to test different spectral analysis procedures, two different 180 day reference numerical data sets have been prepared that mimic the V2 data in terms of integral scale and sampling period and data gap distribution. The data sets are called synthetic turbulence 1 and 2 and were prepared by analogy to a scalar field which has a power spectrum similar to the typical one-dimensional spectrum of a hydrodynamical homogeneous

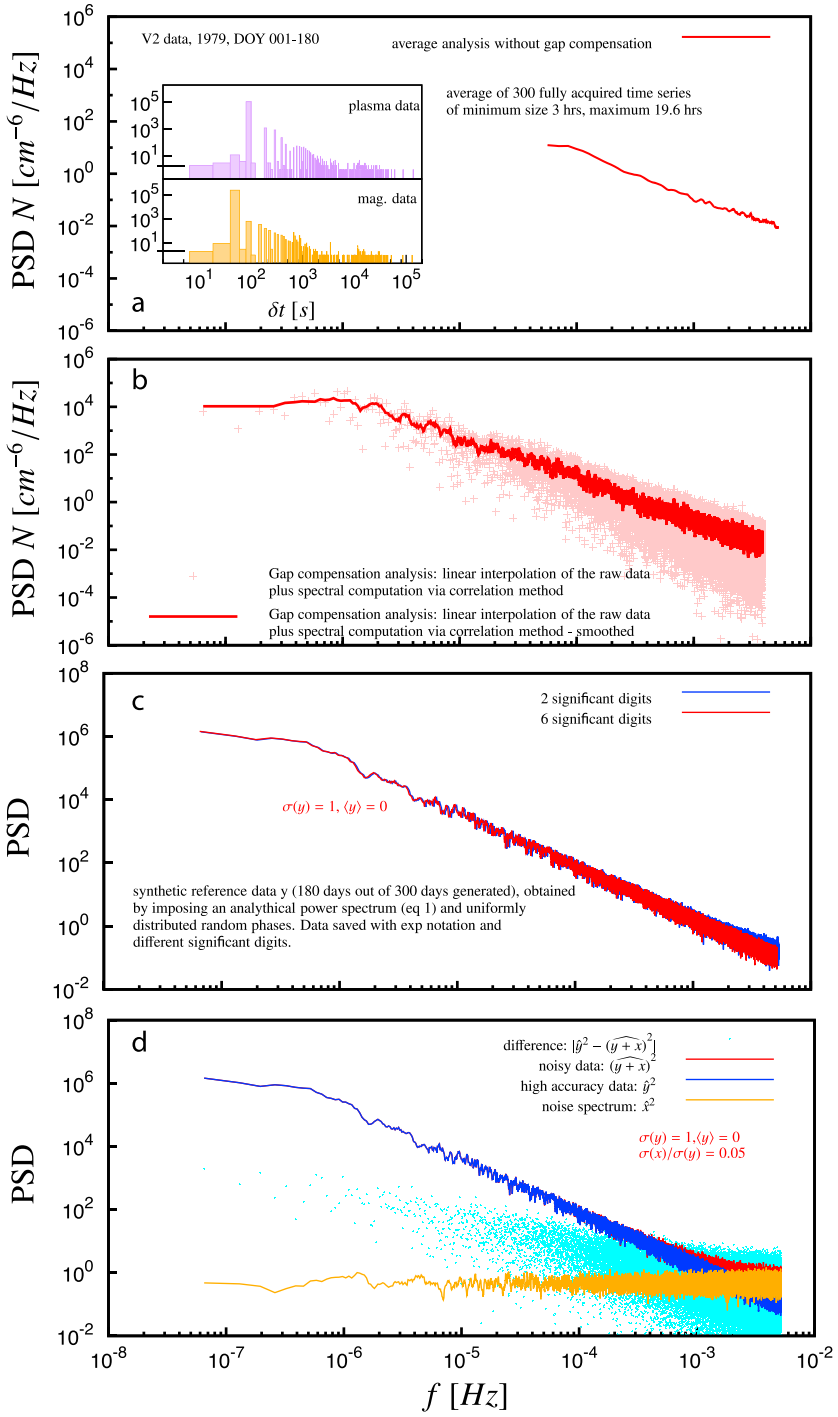

Figure 5. Context of the data sparsity spectral analysis. (a) Averaged density spectrum computed for all the time intervals (3 to 19.6 h) in the first half of 1979 which had no missing data. The inset shows plasma and magnetic field gap distributions. (b) Spectra derived with gap compensation which covers two decades and a half more in frequency range and includes the frequency transition between the energy injection and the interial ranges. This last frequency allows the determination of the system temporal integral scale (see Table 3b). The smoothing used all throughout this work is mild (averages over nine side frequency values) and uniform over all the spectral range to prevent the introduction of spurious results. (c) The minor role played by the precision of the data which is used once a given level of accuracy is obtained. (d) The curtailment of the maximum observable frequency due to the overall confidence level of the measurement and data acquisition chain. The unsmoothed dotted light blue spectrum shows the addition of power spectral energy due to the presence of signal noise.

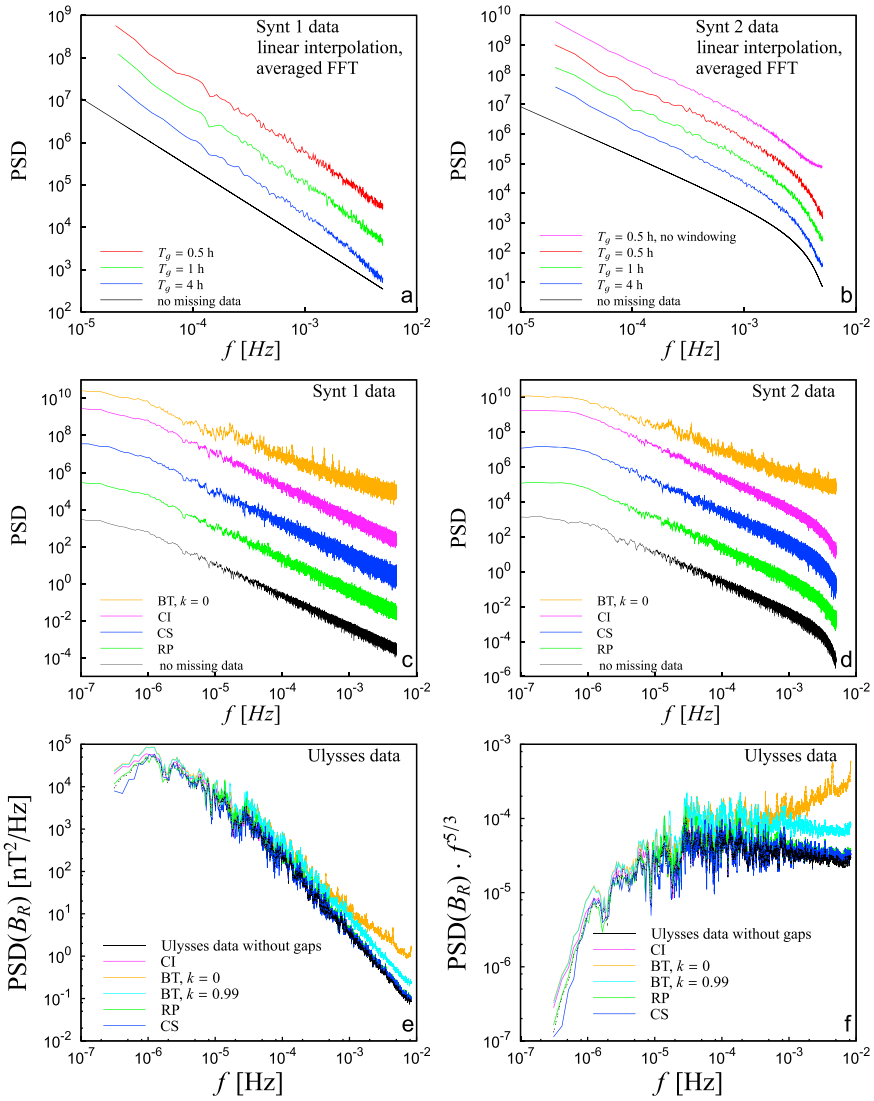

Figure 6. Validation on synthetic data and Ulysses measurement. (a and b) Spectra by direct fast Fourier transform (FFT), with Hann windowing, on linearly interpolated subsets. Segments are selected so that the maximum gap length filled by the interpolation is T_g and their length is at least 12 h. Between 57 and 111 segments have been used for each spectrum. The linear interpolator has a low-pass effect, evident in Figure 6a in the high-frequency range. The error on the spectral index in the range $f \in [10^{-5}, 10^{-3}]$ lies between 1.9% (T_g = 0.5 h) and 5.4% (T_g = 4 h). For the Synt 2 data, windowing helps to recover the correct spectral slopes. Here the error lies between 0.4% (T_g = 0.5 h) and 2.4% (T_g = 4 h) in the range $f \in [10^{-5}, 10^{-3}]$. (c and d) Spectral computation in the entire period. The discrepancy of the power law exponent is below 2.5% for the last three methods (CI, RP, and CS). A smoothing is applied by averaging neighboring frequencies to all curves. The energy is preserved for all spectra, but they have been shifted for clarity. (e and f) Spectrum of the radial component of magnetic field recorded by Ulysses in the period 1990, DOY 298, 1991 DOY 45. The black lines represents the spectrum from Ulysses data. The different spectral recovery methods have been tested after having projected on the Ulysses data the same gap distribution of Voyager 2 data in 1979. (f) The compensated spectrum.

and isotropic turbulent field; see *Monin and Yaglom* [1971]. The two reference fields contain (1) Synt 1: an energy injection range and an inertial range and (2) Synt 2: an energy injection range, an inertial range and a dissipative range.

In these synthetic reference data sets, the energy injection range follows a power law with exponent in the interval 2, the spectral maximum is placed at a frequency corresponding to one solar day, the inertial range extends over three and a half decades and has a power decay equal to −5/3, and the dissipative range is placed around $5 \cdot 10^{-3}$ Hz and has a maximum decay of −3. Furthermore, the phases of the harmonic components have been uniformly randomized.

These sequences have been made sparse by giving them the same gap distribution as the 1979 Voyager 2 data, data sparsity of about the 30%. The true spectra of Synt 1 and 2 (spectra of the complete data sets) are represented with black curves in Figure 6, which illustrates the behavior of the five techniques here considered. The spectral indices are always computed from a linear regression in the log-log space, using all the points of the smoothed spectra within the frequency range we indicate.

Results from the first technique are shown in Figures 6a and 6b for different values of T_g, which is the maximum gap size where data are interpolated. The low-pass behavior of the interpolator results in a steepening of the spectrum, especially in the high-frequency range, and becomes much more evident as T_g increases. For Synt 1, the relative error on the spectral index α lies between 1.9% ($T_g = 0.5$ h) and 5.4% ($T_g = 4$ h) in the range $f \in [10^{-5}, 10^{-3}]$ Hz, while in the last frequency decade it increases up to 8% for $T_g = 0.5$ h. For Synt 2, the discrepancy lies between 0.4% ($T_g = 0.5$ h) and 2.4% ($T_g = 4$ h) in the range $f \in [10^{-5}, 10^{-3}]$ Hz. The Hann windowing is applied to reduce the leakage effect due to the segmentation. Indeed, the purpose is to reduce defects in the FFT output that are introduced by differences in the data at the start and end of the sequence. By comparing the pink and red curves in Figure 6b, one can perceive the windowing effect, which is a reduction of the $\approx 1/f$ noise. Notice that a similar treatment was used by *Bellamy et al.* [2005] where the focus was on large ensemble of "short" spectra from observation periods of about 13 h with maximum missing data of 10%.

The other four techniques allow a spectral recovery over the global frequency range (five decades), see Figures 6c–6f. To all these spectra, a light smoothing has been applied homogeneously over the entire spectral range using a 9-point running average.

We start the discussion by considering the *Blackman and Tukey* [1958] method (BT, in the following), since it has been widely used in solar wind analysis, see, e.g., the works by *Matthaeus and Goldstein* [1982], *Leamon et al.* [1998], *Smith et al.* [2006a, 2006b], *Joyce et al.* [2010], *Borovsky and Denton* [2010], and *Joyce et al.* [2012]. This method is based on the fact that the autocorrelation function and the power spectral density (PSD) are Fourier transform pairs. The strength of this procedure is that it overcomes, in principle, the problem of nonuniform time distribution. Indeed, the 2-point correlation function is obtained by direct application of its definition:

$$C_{ij}^X = \langle X_i(t) X_j(t+\tau) \rangle \rightarrow C_{ij}^X = \frac{1}{N-r} \sum_{n=1}^{N-r} X_i(n) X_j(n+r) \tag{3}$$

where indexes i and j represents the components of the vector $\mathbf{X}$ and $\tau = r\Delta t$ in the discrete case. In the case of missing data, the unknown values can just be ignored, and they do not contribute to the sum (3). The BT method evaluates the 2-point correlation in this way:

$$C_{ij}^X(r) = \frac{1}{N(r)} \sum_{n=1}^{N(r)} X_i(n) X_j(n+r) p(n,r) \quad \text{with} \quad r = 1, \ldots N/2 \tag{4}$$

$$N(r) = \sum_{n=1}^{N} p(n,r) \tag{5}$$

$$p(n,r) = \begin{cases} 1 & \text{if } (n) \text{ and } (n+r) \text{ exist} \\ 0 & \text{if } (n) \text{ or } (n+r) \text{ does not exist} \end{cases} \tag{6}$$

Afterwards, the PSD is then computed by means of a FFT after an (optional) tapered cosine window. Spectra computed in this way are shown in Figures 6c and 6d, orange curves. For the gap amount and distribution of the data we consider, BT does not lead to an accurate spectral estimation. The reason for this resides in the slow convergence of the correlation function, which is highly affected by the sparsity of data when it is computed using (4). The correlations result oscillates, with the same periodicity as the counter $N(r)$, see Figure S1, in the supporting information. The resulting spectra show—for the high data sparsity here considered—nonphysical peaks and biased values of the spectral decay slope; see the orange curves in Figure 6 and subsection 2.1 and Figures 3 and 4.

For Synt 1, the error in the slope is 15.4% for $f \in [10^{-5}, 5 \cdot 10^{-4}]$ Hz and 38% for $f \in [5 \cdot 10^{-4}, 5 \cdot 10^{-3}]$ Hz. For Synt 2, which has a steeper spectrum in this last frequency range, the error goes up to 72%. We conclude therefore that the basic BT method is not suitable for solar wind data with >25% missing data

(at least if the number of points is about 10^5). It should be noted that in all the works cited above, the BT method is shown to work greatly for contiguous data sets or for data sets with at most 10% gaps. Typically, a prewhitening/postdarkening operation is associated to BT, in order to prevent spectral leakage due, e.g., to local trends [see *Rosenblatt*, 1965; *Keisler and Rhyne*, 1976].

The third method we test is still based on the 2-point correlation function. In this case correlations are computed on linearly interpolated data in the entire 180 days period. For gap distribution of V2 data, we show that the linear interpolation improves the convergence of the correlation function; see Figure S1 and Table 1 in the supporting information (SI). The resulting power spectra are the pink curves in Figure 6c and 6d. The linear interpolator has a low-pass effect, leading to a leakage of energy from the higher to the lower frequencies of the spectrum, but in this case this effect is very limited. This is also confirmed by the application of a prewhitening filter, which has no sensible effect on the result. The error in the spectral indices is below 3% for any frequency range.

The fourth procedure is a maximum likelihood data recovery method. This reconstruction is nondeterministic, but it is constrained by the true data where these are available. A complete description of the technique is given by *Rybicki and Press* [1992] and an application can be found in *Press and Rybicki* [1992]. The recovery is based on an estimation of the 2-point correlation function, and it also allows to account for noise in data. We used the same correlations computed for the previous method. In this case the size of filled gaps T_g is a parameter to be chosen, and the goodness of the correlation function allows us to recover the full sequence. Notice indeed that the largest gap is about 45 h, while the correlation function is quite accurate even for much larger time lags (Figure S1 in SI), which allows recovery of the 180 day period. Results are shown in Figure 6c and 6d, green curves. This procedure is computationally more expensive than the others, but it improves the spectral estimation in the high-frequency range by reducing the low-pass effect of the linear interpolator of the previous method. Also, in this case the discrepancy from the correct spectral slope is below 3%.

The last method we show performs a spectral recovery without data interpolation, and it is called *compressed sensing* (CS in the following) [*Donoho*, 2006; *Candes et al.*, 2006a, 2006b]. Results are shown in Figures 6c and 6d, blue curves. CS is a recent theory that provides guarantees for the reconstruction of (exactly or approximately) sparse signals, namely, signals with many null (or approximately null) components, from linear, compressed measurements. In mathematical terms, CS studies the underdetermined linear system $A\mathbf{y} = \mathbf{x}$, where A is matrix of size $m \times n$ with $m < n$ and $\mathbf{y}$ and $\mathbf{x}$ have consistent dimensions. The available data vector $\mathbf{x}$ is then a linear compression of the unknown $\mathbf{y}$, which is assumed to be sparse. CS theory provides conditions that make such problems well posed, that is, with a unique solution. In particular, much effort has been devoted to study which families of sensing matrices A guarantee the possibility of recovery. Among these, partial Fourier matrices (say, discrete Fourier transform matrices with missing rows) have been recently studied [see, e.g., *Rudelson and Vershynin*, 2006; *Duarte and Eldar*, 2011; *Xu and Xu*, 2015], motivated in particular by the applications in medical imaging problems such as magnetic resonance imaging [*Lustig et al.*, 2008]. In the mentioned works, theoretical guarantees on partial Fourier matrices for CS are provided, in terms of the number of necessary measurements and positioning of the missing rows.

The CS approach allows to perform spectral analysis with no previous interpolation of the lacunous data. On the other hand, once the spectrum $\mathbf{y}$ is estimated, one can perform an inversion of the Fourier transform and obtain an estimate of the data without gaps. Moreover, it is also feasible in practice, even when data sets are large. Specifically, in this work we formulated the problem as a Basis Pursuit and obtained the numerical solution through the SPGL1 Matlab solver for sparse problems (see *van den Berg and Friedlander* [2007], for theoretical and practical details). SPGL1 is suitable for the Fourier framework, as it deals with complex variables. Moreover, it allows us to cope with data of large dimension, since the sensing matrix A can be defined as function instead of explicitly storing the whole matrix. The relative error in the spectral slope, with respect to the true value (black curves) for these three methods, is below 2.5%, in the range $f \in [10^{-6}, 5 \cdot 10^{-3}]$ Hz of Synt 1 and $f \in [10^{-6}, 10^{-3}]$ Hz of Synt 2.

To complete this section, an alternative test base with respect to the two synthetic time series SYNT above described was implemented. This test is based on a continuous time series of solar wind measurements from Ulysses data, from DOY 298 1990 to DOY 45 1991, to which the same data gaps previously used have been added. The aim is to check the efficiency of the methods given the three differences between these two test data sets. (1) The SYNT data have random phases; the solar wind data does not. (2) The SYNT data have no inherent periodicities; the solar wind data has the solar rotation and harmonics.

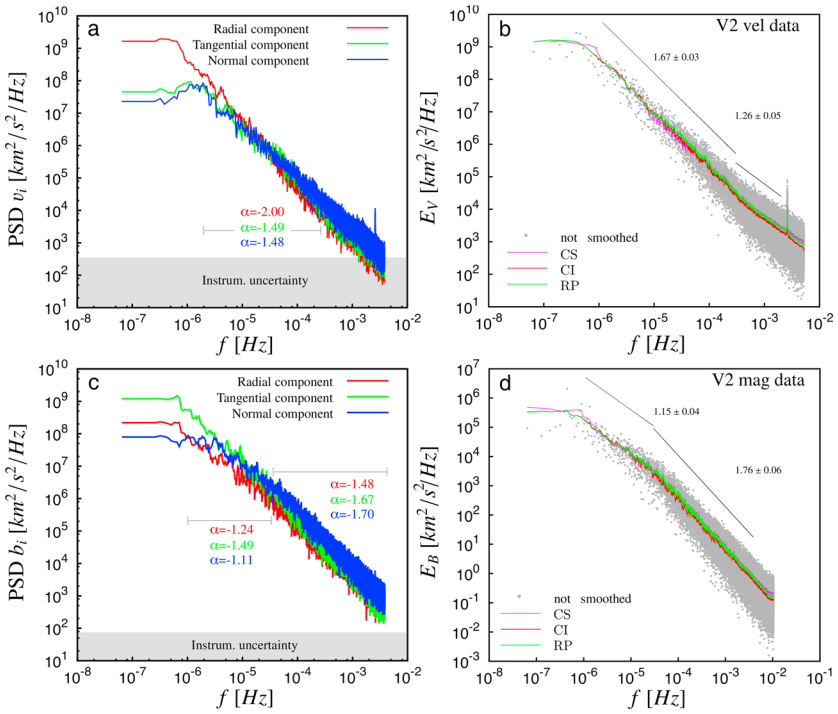

Figure 7. Voyager 2 spectra, 1979, DOY 1–180. (a) Spectra of the velocity plasma components computed by the correlations method with linear interpolation. (b) Spectrum of the plasma kinetic energy. Three methods of analysis (compressed sensing, correlation spectrum with linear interpolation and Rubycki & Press maximum likelihood recovery) are compared. (c and d) Same as Figures 7a and 7b for the magnetic field. The grey bands in Figures 7a and 7c indicate the instrumental uncertainty. The grey curve in Figures 7b and 7d represents the unsmoothed spectrum by means of interpolated correlations. The spectral exponents are reported in Table 3a.

(3) The SYNT data has a single spectral index all the way to the 27 day solar rotation period; the solar wind data has a spectral breakpoint in the vicinity of several hours. The results of the second test are shown in Figures 6e and 6f. One can see that the various techniques perform in substantially the same way as they do with the synthetic time series.

3.1. Plasma and Magnetic Field Spectra

The spectra obtained for each component of magnetic field and plasma velocity and for their relevant energy are represented in Figure 7. Leaving aside the BT method with no prewhitening, it should be noted that all the gap recovery methods converge at similar exponent and can be considered equivalent. In what follows we chose to present here the results given by the correlation method with linear interpolation.

Looking at the power spectra of each component of the velocity field, shown in Figure 7a and resumed in Table 3a, the behavior of the system at low frequencies ($f < 4 \cdot 10^{-4}$) shows that the exponent is steeper for the radial component than for the other two. In particular, the spectral index in the radial direction is $\alpha_{v_R} \approx -2.00$. At high frequencies, the situation is reversed and the spectral index of the radial component is $\alpha_{v_R} \approx -1.18$, smaller than the other two ($\alpha_{v_T} \approx -1.28$, $\alpha_{v_N} \approx -1.48$). Considering the power spectrum of the kinetic energy, the exponent found is $\alpha_{E_k} \approx -1.67$ in the low-frequency domain. Such a value is consistent with the Kolmogorov hydrodynamic theory for isotropic turbulence, which predicts an exponent of −5/3 [see also *Marsch and Tu*, 1989]. In the high-frequency range, for $f \in [3 \cdot 10^{-4}, 2 \cdot 10^{-3}]$ the fit gives the value of $\alpha_{E_k} \approx -1.33$.

However, caution must be taken before adopting the Kolmogorov interpretation because a given spectral power law can represent different phenomenology, and leaving aside the peculiar anisotropy of the solar wind, there are physical arguments that contradict this hypothesis. For instance, by estimating the eddy turn over time on the basis of the frequency where the inertial cascade seems to initiate (frequency of $1 \cdot 10^{-6}$ Hz, which is a period of $1 \cdot 10^6$ s), the solar advection speed and the intensity of the turbulent fluctuations (same order as the Alfvén speed) one gets too large an eddy turnover time, as high as 5 times the age of the plasma.

Table 3a. Solar Wind Spectral Exponents From Voyager 2 Data[a]

	Spectral Index			
f Range	v_R	v_T	v_N	E_v
$10^{-6} \div 4 \cdot 10^{-4}$	−2.00	−1.49	−1.48	−1.67
$4 \cdot 10^{-4} \div 5 \cdot 10^{-3}$	−1.18	−1.26	−1.48	−1.33
B_R	B_T	B_N	E_B	
$1 \cdot 10^{-6} \div 3 \cdot 10^{-5}$	−1.06	−1.46	−0.85	−1.21
$3 \cdot 10^{-5} \div 5 \cdot 10^{-3}$	−1.56	−1.72	−1.77	−1.72
	b_R	b_T	b_N	E_b
$10^{-6} \div 3 \cdot 10^{-5}$	−1.24	−1.49	−1.11	−1.34
$3 \cdot 10^{-5} \div 5 \cdot 10^{-3}$	−1.48	−1.67	−1.70	−1.65

[a]The maximum error on spectral indexes is about 0.07; b is the magnetic field in Alfvén units.

So that at these frequencies, the Voyager 2 spectrum cannot be due to active turbulence. In fact, by observing Figure 7a, one can see that the low-frequency velocity spectrum is dominated by the Fourier power of the radial component which can be associated with remnant variations of the solar wind speed near the Sun that are equilibrating at 5 AU owing to fast and slow parcels interacting. Moreover, the low-frequency magnetic field spectrum in Figure 7b is dominated by the tangential component which is associated with variations to the field strength owing to compressions and rarefactions of the toward-and-away Parker spiral field by those same slow-versus-fast wind interactions.

However, it should also be noticed that the fluctuation series of v_R and B_T (see NASA database at http://omniweb.gsfc.nasa.gov/coho/) [*NASA Goddard Space Flight Center*, 2016] show a change of slope at about $2 \cdot 10^{-5}$ Hz (13.8 h) and $4 \cdot 10^{-5}$ Hz (7 h), respectively, where the contribution of the jumps is lower than 40%. Considering velocity fluctuations of 30 km/s, these frequencies can correspond to structures with a size of 0.15 AU or 0.075 AU and related turnover times of 9 days and 4.5 days. These relatively small values leave open the possibility that such fluctuations could be owed to active turbulence. Could this fluctuation range be owed to active turbulence? In principle, yes. But not all fluctuations are turbulent. Wave fluctuations are extensively present as well. And another question is pending: can an integral scale of the order of one to tens of AU be consistent with a mean free path of the order of 1–2 AU [*Cummings and Stone*, 1999]?

We also observe a flattening in the velocity spectra at high frequencies. This trend has been observed by other authors [*Matthaeus and Goldstein*, 1982; *Roberts*, 2010]. The first paper pointed out that the flattening may be due to aliasing, but the second paper excluded this hypothesis. This flattening was also found for the proton density and temperature fluctuations [*Marsch and Tu*, 1990a], as well as for the Elsässer variables [*Marsch and Tu*, 1990b]. It is most typical of high-speed streams below 1 AU, in these cases the frequency range is more extended and the change of slope occurs at $f \approx 10^{-7}$. Here we cannot exclude that the flattening in the velocity spectra is partially due to the level of noise in the data. The instrumental uncertainty on the velocity components is about ±2 km/s. Modeling this as a uniform noise of amplitude ±2 km/s, we observe from the synthetic reference that this could influence the last spectral decade (see Figure 5). We have also checked

Table 3b. Temporal Scales From Voyager 2 Data[a]

Variables	Description	Value	Unit
T_{E_v}	Kinetic macroscale	26.8	days
T_{E_m}	Magnetic macroscale	25.9	days
T_N	Density macroscale	13.1	days
T_{vth}	Thermal speed macroscale	11.0	days
T_{Hc}	Cross-helicity macroscale[b]	25.1	days
τ_v	Kinetic Taylor microscale	1.54	h
τ_m	Magnetic Taylor microscale	0.85	h
τ_N	Density Taylor microscale	1.04	h
τ_{vth}	Thermal speed Taylor microscale	0.85	h
τ_{Hc}	Cross-helicity Taylor microscale[b]	5.17	h

[a]T and τ are the integral scale and the Taylor microscale, deduced from the spectra as $T = \int_0^{+\infty} E(f)/f\mathrm{d}f / \int_0^{+\infty} E(f)\mathrm{d}f$ and $\tau^2 = \int_0^{+\infty} E(f)\mathrm{d}f / \int_0^{+\infty} f^2 E(f)\mathrm{d}f$, where $E(f)$ is the spectrum of the relevant quantity.
[b]*Iovieno et al.* [2016].

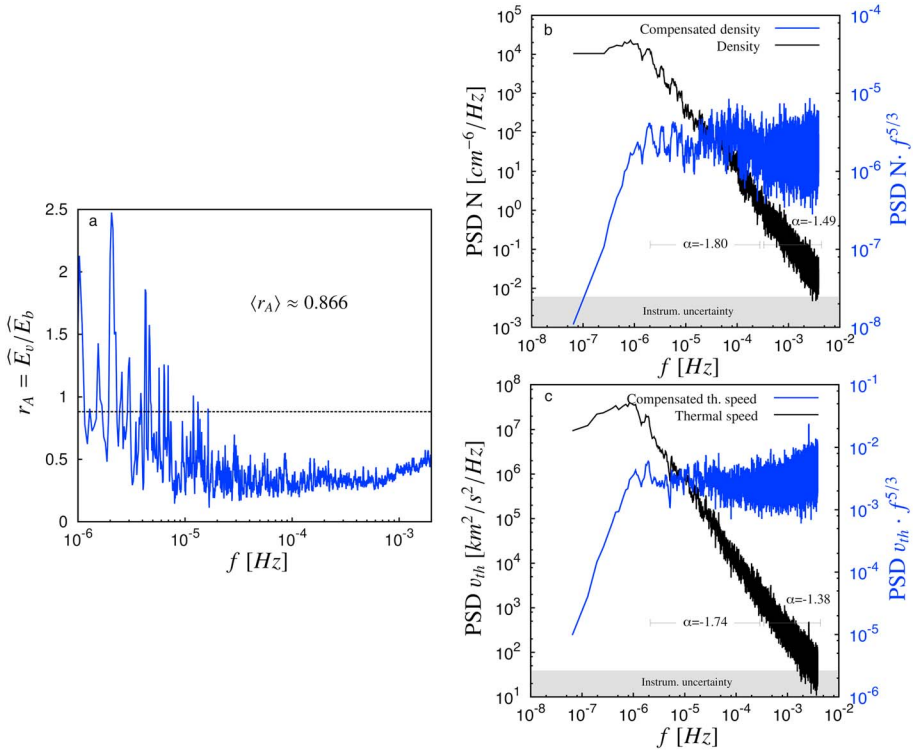

Figure 8. (a) Spectral distribution of the Alfvén ratio $\widehat{r}_A$. The differences between the slopes of the spectra of plasma velocity and magnetic field lead to a gradual reduction of the Alfvén ratio for increasing frequencies: r_A is lower than 0.5 for all frequencies above 10^{-5} Hz. This is in overall agreement with other analysis of the slow solar wind [*Marsch and Tu*, 1990b]. (b and c) Density and thermal speed spectra.

the leakage hypothesis by applaying the first difference prewhitening filter to the correlation method and by using the second structure function. We verified that both the correlation function and the structure function converge on linearly interpolated data (160,000 points) and that the application of the prewhitening filter does not change the results when correlations are used. The relative difference in the spectra computed with and without PW remains below 1% for all frequencies.

The magnetic field components (Figure 7c) present a very different phenomenology with respect to the plasma velocity: for each component the spectra have higher exponents in the high-frequency range ($f > 3 \cdot 10^{-5}$) and they tend to become flatter at low frequencies, as shown in Figure 7c and 7d and in Table 3a. Moreover, an anisotropic behavior is also observed both at high and low frequencies: in particular, the radial component is always lower than the tangential one. The normal component, instead, has a spectral index analogous to the radial one a low frequencies (for $f < 3 \cdot 10^{-5}$, considering Alfvén units, $\alpha_{b_R} \approx -1.24$ and $\alpha_{b_N} \approx -1.11$, when $\alpha_{b_T} \approx -1.49$), while it becomes similar to the tangential exponent at high frequencies (for $f > 3 \cdot 10^{-5}$, considering Alfvén units, $\alpha_{b_T} \approx -1.67$ and $\alpha_{b_N} \approx -1.70$, when $\alpha_{b_T} \approx -1.48$).

The spectral exponent for the magnetic energy is $\alpha_{E_m} \approx -1.65$ at high frequencies, as predicted by the Kolmogorov law (Figure 7d). At low frequencies the exponents drop to values around $\alpha_{E_m} \approx 1.34$.

The different behavior of the power spectra of kinetic and magnetic energies can be appreciated by considering the Alfvén ratio, defined as

$$\widehat{r}_A(f) = \frac{\widehat{E}_v(f)}{\widehat{E}_b(f)} \tag{7}$$

and represented in Figure 8a.

The Alfvén ratio is usually less than unity in the inertial range [*Tu and Marsch*, 1995; *Matthaeus and Goldstein*, 1982]. Moreover, the minimum value is lower than 0.5, as observed for slow solar wind inside 1 AU [*Orlando et al.*, 1997]. In general, leaving aside the frequency of the minimum which depends on the distance from the Sun, similar evolution of $\hat{r}_A$ with frequency can be observed [*Marsch and Tu*, 1990b]. For completeness, in Figures 8b and 8c, spectra of the density and thermal speed are reported. The behavior is similar for the integral scale and inertial decay in the central part. A light steepening of the inertial decay is observed for the thermal speed analogous to that of the plasma normal component.

4. Conclusions

In this work we computed the power spectra of the solar slow wind, density, thermal speed, and magnetic field at 5 AU at low latitude from Voyager 2 measurements. By using data reconstruction techniques to overcome high rate of missing data issues, in particular the underestimation of the spectral decay and the presence of spurious peaks, we have been able to determine spectra for a frequency range extending over five decades ($10^{-7}-10^{-2}$ Hz). This extended range, much wider than in any other previous study at this distance, allows us to observe the changes in the spectral slopes providing information on the structure of the solar wind. The analysis procedures have been validated by testing five different data recovery methods (windowed averaged Fourier transforms of short data subsets, linearly interpolated over short gaps, Blackman-Tukey method, linear interpolation plus 2-point correlations, and maximum likelihood recovery and compressed sensing) both on synthetic data which mimic the behavior of the well-known homogeneous and isotropic turbulence system and on a continuous time series of solar wind measurements from 1 AU, to which data gaps have been added. In particular, the two test bases have been made lacunous by projecting the same gap distribution as in the 1979 first semester V2 plasma data.

The plasma velocity spectrum presents an intermediate frequency range with a power law decay exponent of about -2 for the radial component and of about -1.5 for the tangential and normal components up to $f = 3\cdot10^{-4}$ Hz, while some flattening occurs at higher frequencies. The magnetic spectrum shows a change of spectral index at about $f = 5\cdot10^{-5}$ Hz, in agreement with Ulysses data near the ecliptic at 4.8 AU. Above this frequency the slope is -1.76 ± 0.06 and remains constant in the whole range of observed frequencies. We can therefore conclude that the inertial range extends at least from $f = 5\cdot10^{-5}$ to $f = 5\cdot10^{-3}$ Hz. The variation of the spectral index can be due to the presence of Alfvén waves or to anisotropies with relevant effects of the parallel sweeping due to the large-scale magnetic fluctuations. In fact, the anisotropy appears to be significant at frequencies below $f = 10^{-5}$ Hz, when most of the energy tends to be concentrated into the radial component of the velocity fluctuations and in the tangential component of the magnetic field fluctuations. Moreover, the Alfven ratio, which remains small for most of the frequency range, becomes larger than 0.5 at the lowest frequencies, below $f = 10^{-5}$ Hz. At high frequencies there is a marked dominance of magnetic energy with respect to kinetic energy.

For all the gap compensation methods here presented, practical details concerning software issues are described in the supporting information.

Acknowledgments

We would like to thank the two anonymous referees for providing us with constructive comments and suggestions. This collaboration between the Politecnico di Torino and MIT was sponsored by the Progretto MITOR with support by the Fondazione Compagnia Di San Paolo. J.D.R. was supported by NASA under the Voyager project. Supporting information on data processing routines are included in the SI file; further information can be obtained from D.T. (email: daniela.tordella@polito.it). SF and EM acknowledge support from European Community's Seventh Framework Programme (FP7/2007-2013)/ERC grant agreement 279848.

References

Behannon, K. W., M. H. Acuna, L. F. Burlaga, R. P. Lepping, N. F. Ness, and F. M. Neubauer (1977), Magnetic field experiment for Voyagers 1 and 2, *Space Sci. Rev.*, *21*(3), 235–257.

Bellamy, B. R., I. H. Cairns, and C. W. Smith (2005), Voyager spectra of density turbulence from 1 AU to the outer heliosphere, *J. Geophys. Res.*, *110*, A10104, doi:10.1029/2004JA010952.

Blackman, R. B., and J. W. Tukey (1958), *The Measurement of Power Spectra*, Dover Publ., New York.

Borovsky, J. E., and M. H. Denton (2010), Solar wind turbulence and shear: A superposed epoch analysis of corotating interaction regions at 1 AU, *J. Geophys. Res.*, *115*, A10101, doi:10.1029/2009JA014966.

Bridge, H. S., J. W. Belcher, R. J. Butler, A. J. Lazarus, A. M. Mavretic, J. D. Sullivan, G. L. Siscoe, and V. M. Vasyliunas (1977), The plasma experiment on the 1977 Voyager mission, *Space Sci. Rev.*, *21*, 259–287.

Bruno, R., and V. Carbone (2013), The solar wind as a turbulence laboratory, *Living Rev. Solar Phys.*, *2*, 4, doi:10.12942/lrsp-2005-4.

Candes, E. J., J. K. Romberg, and T. Tao (2006a), Robust uncertainty principles: Exact signal reconstruction from highly incomplete frequency information, *IEEE Trans. Inf. Theor.*, *52*(2), 489–509, doi:10.1109/TIT.2005.862083.

Candes, E. J., J. K. Romberg, and T. Tao (2006b), Stable signal recovery from incomplete and inaccurate measurements, *Commun. Pure Appl. Math.*, *59*(8), 1207–1223, doi:10.1002/cpa.20124.

Cummings, A. C., and E. C. Stone (1999), Radial interplanetary mean free paths inferred from anomalous cosmic ray observations in the outer heliosphere, in *Proceedings of the 26th International Cosmic Ray Conference*, vol. 7, pp. 496–499, Int. Union of Pure and Appl. Phys., Salt Lake City, Utah.

Donoho, D. L. (2006), Compressed sensing, *IEEE Trans. Inf. Theory*, *52*(4), 1289–1306, doi:10.1109/TIT.2006.871582.

Duarte, M., and Y. Eldar (2011), Structured compressed sensing: From theory to applications, *IEEE Trans. Signal Process.*, *59*(9), 4053–4085, doi:10.1109/TSP.2011.2161982.

Fraternale, F., L. Gallana, M. Iovieno, M. Opher, J. D. Richardson, and D. Tordella (2016), Turbulence in the solar wind: Spectra from Voyager 2 data at 5 AU, *Phys. Scr.*, *91*(2), 394–401, doi:10.1088/0031-8949/91/2/023011.

Horbury, T. S., and B. Tsurutani (2001), Ulysses measurements of waves, turbulence and discontinuities, in *The Heliosphere Near Solar Minimum: The Ulysses perspective*, edited by A. Balogh, R. G. Marsden, and E. J. Smith, pp. 167–227, Springer-Praxis Books in Astrophys. and Astron., London.

Iovieno, M., L. Gallana, F. Fraternale, J. D. Richardson, M. Opher, and D. Tordella (2016), Cross and magnetic helicity in the outer heliosphere from Voyager 2 observations, *Eur. J. Mech. B/FluidsS*, *55*(2), 394–401, doi:10.1016/j.euromechflu.2015.08.009.

Joyce, C. J., C. W. Smith, P. A. Isenberg, N. Murphy, and N. A. Schwadron (2010), Observation of bernstein waves excited by newborn interstellar pickup ions H^+ and He^+ as seen by Voyager at 4.5 AU, *Astroph. J.*, *724*, 1256–1261.

Joyce, C. J., C. W. Smith, P. A. Isenberg, S. P. Gary, N. Murphy, P. C. Gray, and L. F. Burlaga (2012), Observation of bernstein waves excited by newborn interstellar pickup ions in the solar wind, *Astroph. J.*, *745*, 112–120.

Keisler, S. R., and R. H. Rhyne (1976), An assessment of prewhitening in estimating power spectra of atmospheric turbulence at long wavelengths, *Nasa Technical Note D-8288*, Natl. Aeronaut. and Space Admin., Washington, D. C.

Leamon, R., C. Smith, N. Ness, W. Matthaeus, and H. Wong (1998), Observational constraints on the dynamics of the interplanetary magnetic field dissipation range, *J. Geophys. Res.*, *103*(A3), 4775–4787, doi:10.1029/97JA03394.

Lustig, M., D. Donoho, J. Santos, and J. Pauly (2008), Compressed sensing MRI, *IEEE Signal Process. Mag.*, *25*(2), 72–82, doi:10.1109/MSP.2007.914728.

Marsch, E., and C. Tu (1989), Dynamics of correlation-functions with elasser variables for inhomogeneous MHD turbulence, *J. Plasma Phys.*, *41*, 479–491.

Marsch, E., and C.-Y. Tu (1990a), Spectral and spatial evolution of mhd turbulence in the inner heliosphere, *J. Geophys. Res.*, *95*(14), 11,945–11,956.

Marsch, E., and C.-Y. Tu (1990b), On the radial evolution of mhd turbulence in the inner heliosphere, *J. Geophys. Res.*, *95*(A6), 8211–8229, doi:10.1029/JA095iA06p08211.

Matthaeus, W. H., and M. L. Goldstein (1982), Measurement of the rugged invariants of magnetohydrodynamic turbulence in the solar wind, *J. Geophys. Res.*, *87*(NA8), 6011–6028, doi:10.1029/JA087iA08p06011.

Monin, A. S., and A. M. Yaglom (1971), *Statistical Fluid Mechanics*, vol. 2, MIT Press, Cambridge, Mass.

Montgomery, D., M. Brown, and W. Matthaeus (1987), Density fluctuation spectra in magnetohydrodynamic turbulence, *J. Geophys. Res.*, *92*(A1), 282–284, doi:10.1029/JA092iA01p00282.

NASA Goddard Space Flight Center (2016), Deep space hourly and daily merged magnetic field, plasma, proton fluxes and ephemerides data, Greenbelt, Md. [Available at http://omniweb.gsfc.nasa.gov/coho/, accessed 1 March 2016.]

Orlando, S., Y. Lou, G. Peres, and R. Rosner (1997), Alfvénic fluctuations in fast and slow solar winds, *J. Geophys. Res.*, *102*(A11), 24,139–24,149, doi:10.1029/97JA01988.

Podesta, J. J., D. A. Roberts, and M. L. Goldstein (2007), Spectral exponents of kinetic and magnetic energy spectra in solar wind turbulence, *Astrophys. J.*, *664*, 543–548, doi:10.1086/519211.

Press, W. H., and G. B. Rybicki (1992), The time delay of gravitational lens 0957+561. I. Methodology and analysis of optical photometric data, *Astroph. J.*, *385*, 404–415, doi:10.1086/170951.

Roberts, D. A. (2010), Evolution of the spectrum of solar wind velocity fluctuations from 0.3 to 5 AU, *J. Geophys. Res.*, *115*, A12101, doi:10.1029/2009JA015120.

Rosenblatt, H. M. (1965), *Spectral Analysis and Parametric Methods for Seasonal Adjustment of Economic Time Series*, U.S. Dep. of Commerce, Bureau of the Census, vol. 23, pp. 235–257, Washington, D. C.

Rudelson, M., and R. Vershynin (2006), Sparse reconstruction by convex relaxation: Fourier and Gaussian measurements, in *40th Annual Conference of Information Sciences and Systems (CISS)*, vols. 1–4, pp. 207–212, Princeton Univ., Dept. Elect. Engn.; IEEE Informat Theory Soc., Princeton, N. J., doi:10.1109/CISS.2006.286463.

Rybicki, G. B., and W. H. Press (1992), Interpolation, realization, and reconstruction of noisy, irregularly sampled data, *Astroph. J.*, *398*, 169–176, doi:10.1086/171845.

Smith, C. W., K. Hamilton, B. J. Vasquez, and R. J. Leamon (2006a), Dependence of the dissipation range spectrum of interplanetary magnetic fluctuations upon the rate of energy cascade, *Astroph. J. Lett.*, *645*, L85–L88, doi:10.1086/506151.

Smith, C. W., B. J. Vasquez, and K. Hamilton (2006b), Interplanetary magnetic fluctuation anisotropy in the inertial range, *J. Geophys. Res.*, *111*, A09111, doi:10.1029/2006JA011651.

Tu, C.-Y., and E. Marsch (1995), MHD structures, waves and turbulence in the solar wind: Observations and theories, *Space Sci. Rev.*, *73*(1–2), 1–210, doi:10.1007/BF00748891.

van den Berg, E., and M. P. Friedlander (2007), SPGL1: A solver for large-scale sparse reconstruction, University of British Columbia, Vancouver, Canada. [Available at http://www.cs.ubc.ca/labs/scl/spgl1, accessed 1 March 2016.]

Xu, G., and Z. Xu (2015), Compressed sensing matrices from Fourier matrices, *IEEE Trans. Inf. Theory*, *61*(1), 469–478, doi:10.1109/TIT.2014.2375259.